


Elastic Metasurface with Dual-Coupled Resonators for Highly Efficient Energy Harvesting

Tian Yang,^{1,‡} Zibin Lin,^{2,‡} Xuefeng Zhu^{2,*} and Tianzhi Yang^{1,†}

¹*School of Mechanical Engineering and Automation, Northeastern University, Shenyang, 110819, China*

²*School of Physics and Innovation Institute, Huazhong University of Science and Technology, Wuhan 430074, China*

 (Received 20 September 2022; revised 24 October 2022; accepted 22 November 2022; published 21 December 2022)

Highly efficient elastic wave manipulation is crucial in the materials and physical engineering communities. Recently, coupling-interaction theory has attracted extensive attention to enhance the efficiency of traditional metamaterials. Here, experimental demonstrations of an elastic focusing metasurface with a dual-coupled resonator for high-efficient energy harvesting are exhibited. An easy-to-implement optimized elastic metasurface with bridged coupling, which is higher efficiency than traditional elastic metasurfaces, is proposed. Results show that a significantly enhanced efficiency, up to 239% is achieved, compared with a conventional metasurface. Furthermore, the robustness of the enhanced efficiency against variation of the focal point and frequency fluctuations of the incident waves is observed. The suggested device provides a simple feasible method for high-efficient energy harvesting.

DOI: [10.1103/PhysRevApplied.18.064065](https://doi.org/10.1103/PhysRevApplied.18.064065)

I. INTRODUCTION

In recent years, metamaterials have exhibited excellent capabilities in controlling the wave front [1–6]. As an important member of this family, elastic metamaterials are presented for advanced elastic wave manipulation [7–17]. Many exotic elastic wave behaviors have been realized according to the generalized Snell law (GSL) [18]. However, the local power-flow conservation of the GSL is an invalid assumption. Most previous traditional elastic metasurfaces (EMs) based on this local design strategy reach a relatively low efficiency. As a consequence, the incident energy cannot be transferred to the target direction perfectly. It means that unexpected scattering and side lobes are nearly unavoidable based on the GSL. Therefore, it is further suggested that strong coupling-interaction ideas are introduced to improve the control capabilities of elastic metasurfaces [19–25]. In this regime, the energy is allowed to tunnel and adjust between microstructures so that the efficiency of the optimized EM is enhanced greatly. Not limited to elastic metamaterials, most coupled designs rest on complex and delicate optimization algorithms or extensive and numerous theoretical calculations [21,26]. Indeed, most of these designs are difficult to implement and manufacture.

Here, we present the facile fabrication of an optimized EM with a dual-coupled resonator that can achieve energy harvesting. By introducing strong bridged couplings simply, the independent mass oscillators in each unit cell of the traditional EM are connected. A high-efficiency energy focusing of the EM with coupling-interaction characteristics is experimentally observed compared with the efficiency of a conventional EM based on the GSL. The tailored coupling bridges are easy to implement and manufacture. Furthermore, the high efficiency of an optimized EM with a dual-coupled resonator can be maintained when the focal point is within the range of $20 \times 40 \text{ cm}^2$, and the robustness of the enhanced efficiency against frequency fluctuations in the range of 34.5–36.5 kHz of the incident waves is observed.

II. TRADITIONAL DESIGN AND OPTIMIZED COUPLING DESIGN

As illustrated in Fig. 1, highly efficient energy harvesting of the optimized EM with a dual-coupled resonator is realized by introducing strong bridged couplings into the traditional EM. Based on the GSL, the phase gradient is modulated in the local EM as follows:

$$\frac{\sin(\theta_t)}{\lambda} - \frac{\sin(\theta_i)}{\lambda} = \frac{1}{2\pi} \frac{d\varphi(x)}{dx}, \quad (1)$$

where $d\varphi(x)/dx$ is the correlation term of the phase gradient along the interface. θ_t and θ_i are the transmitted and incident angles of flexural waves, respectively. Here

*xfzhu@hust.edu.cn

†yangtianzhi@me.neu.edu.cn

‡T. Yang and Z. Lin contributed equally to this work.

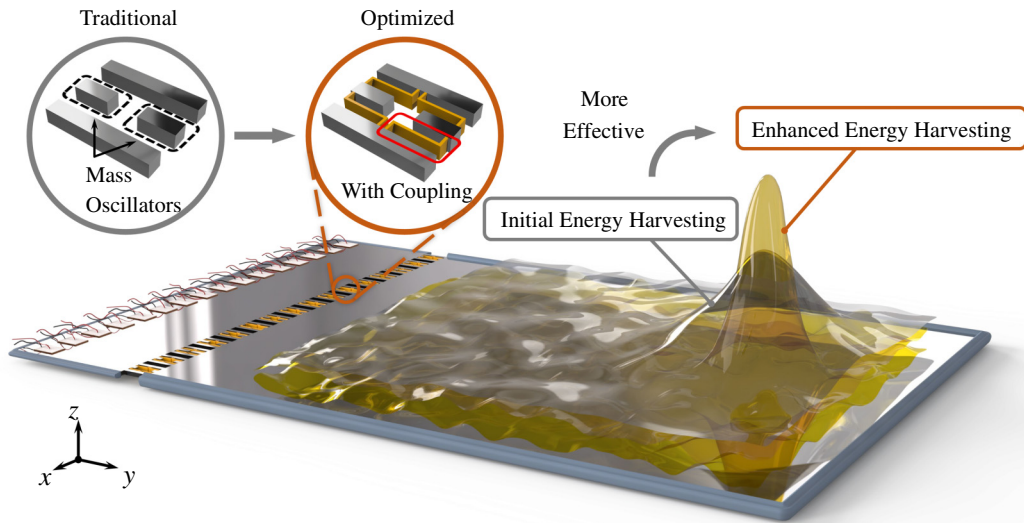


FIG. 1. Schematic of high-efficiency elastic energy harvesting.

$\lambda = c_p/f$ is the wavelength with the ordinary frequency, f , and $c_p = [E\omega^2(H/2)^2/3\rho(1-\nu^2)]^{1/4}$ is the wave velocity. ω is the angular frequency, and H is the thickness of the plate. E , ρ , and ν are the elastic modulus, mass density, and Poisson ratio, respectively. As shown in the inset of Fig. 1, a unit cell includes two symmetrical and independent mass oscillators of the same size in the conventional EM. Each mass oscillator can be regarded as a single-degree-of-freedom mass-spring system. Modulation of the required phase gradient is realized by adjusting the length parameters of the two mass oscillators synchronously. However, mass oscillators of the traditional design vibrate separately from each other. This means that strong couplings between microstructures are discarded in the conventional EM. The efficiency is quite low for the traditional local response.

To enhance the efficiency, a coupling interaction is induced in the metasurfaces by creating strong bridged couplings simply between microstructures in each unit cell, as shown in the inset of Fig. 1. As a result, a high-efficiency optimized EM with extra paths for energy tunneling is obtained. A coupling relationship is introduced to govern the propagation of elastic waves across the surface between the microstructures in the optimized EM so that the energy is efficiently transferred to the destination [19,23–25]. Notably, coupling interactions are introduced into the metasurfaces by creating bridges between microstructures in each cell. Mass oscillators are changed from previously independent to closely related in each unit cell to improve efficiency. This process can be regarded as connecting several masses of spring systems to control the energy transmission more stably and effectively. Consequently, compared to the conventional EM with

independent vibrations, energy interactions take place in each unit cell of the optimized EM. To further uncover the highly efficient mechanisms, the distribution of power flow is analyzed inside both unit cells, as shown in Appendix A. Coupling bridges between the oscillator transmit the twisting moment from the oscillator to the neighboring links. A smoother and more stable energy flow is obtained to improve the efficiency of the EM based on the vibrational energy interaction in the coupled bridge tunnels. It ought to be clarified that couplings exist between the resonators, but the optimized EM is still a local device. Coupling occurs inside a unit cell and the microstructures are linked together for excellent transmission efficiency, which is along the propagating direction. In this regime, the coupling interaction plays an essential role in enhancing the efficiency of the EM with a dual-coupled resonator.

Specifically, to evaluate the relationship between the phase shift and width of the weight, l , the finite-element software COMSOL Multiphysics is used for modeling and simulation. The traditional EM and optimized EM are both composed of aluminum. The properties and geometric parameters of the materials are shown in Appendix B. As shown in Fig. 2(a), a variation of the elastic wave phase shift with l for $f = 34.8\text{--}38.2$ kHz is obtained. Compared with the conventional design, a phase shift of 2π is nearly covered for the optimized elastic waves. Notably, a phase shift with smooth and enhanced continuity is realized. This means that the size distribution of each functional unit is uniform and easily distinguishable, which is important for manufacturing. Whereas, a phase shift with poor continuity and severe abrupt changes is observed in the traditional functional unit. Moreover, the results of the vertical comparison strongly suggest that the capabilities of

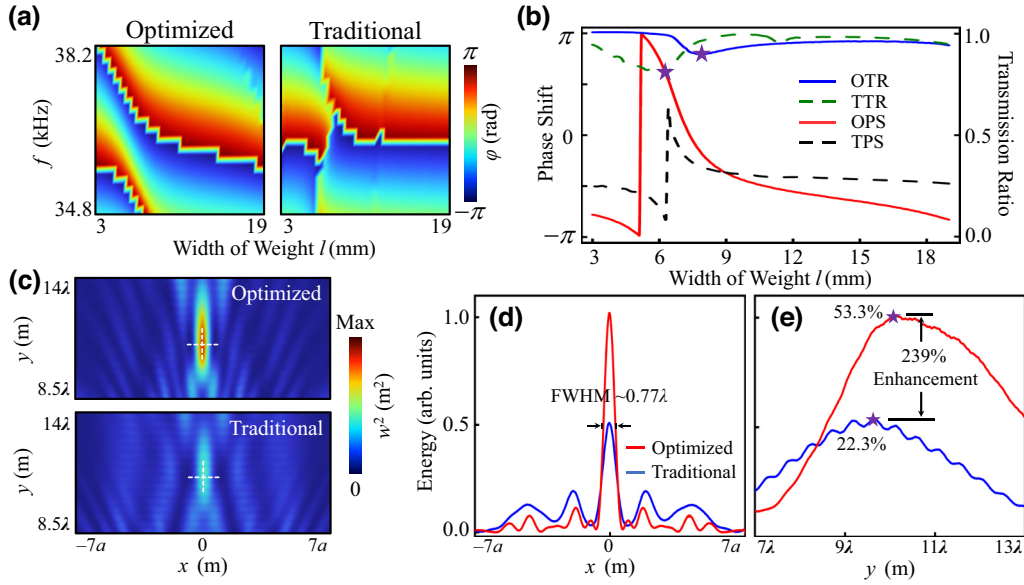


FIG. 2. Comparison of the functional units and energy focusing. (a) Phase shift for $f = 34.8\text{--}38.2$ kHz. (b) At 35.5 kHz, the black dashed line and red solid line represent the traditional (TPS) and optimized phase shift (OPS), and the green dashed line and blue solid line represent the traditional (TTR) and optimized transmission ratio (OTR). Minimum transmission ratios for traditional and optimized unit cells are 80.1% and 89.4%, respectively, as marked with purple stars. (c) Intensity distribution of displacement-focusing fields at 35.5 kHz. (d),(e) Energy distribution of focal points horizontally and vertically at 35.5 kHz, respectively. Efficiency of the traditional EM and optimized EM is 22.3% and 53.3%, respectively, as marked with purple stars in (e).

the optimized design are not sensitive to frequency variation. In the subsequent case, the coupled device shows robustness to frequency fluctuations over the range of 34.5–36.5 kHz. Without losing generality, an initial excitation at $f = 35.5$ kHz is randomly selected for further comparison and experiments. As shown in Fig. 2(b), the change of the red solid line is flatter than the black dashed line. The optimized design with a dual-coupled resonator has more moderate phase shifts and higher transmission ratios than the conventional design.

III. RESULTS AND DISCUSSION

In our example, initial incident waves ($\theta_i = 0^\circ$) at $f = 35.5$ kHz are excited to compare the efficiency for focusing of the traditional and optimized designs under normal incidence along the y direction. Conventional elastic focusing can be realized by adjusting the phase gradient of functional unit cells. The phase gradient $d\phi(x)$ can be provided as

$$\phi(x) = \vec{k}_i \cdot \overline{PS} = \frac{2\pi}{\lambda} \left(\sqrt{f_y^2 + (x - f_x)^2} - f_y \right), \quad (2)$$

where \vec{k}_i is the wave vector, \overline{PS} is the distance needed to be compensated for to realize focusing, f_y is the focal length, and f_x is the distance from the focal point to the central axis of metasurfaces along the x direction. To achieve focusing with an initial focal point located at $(f_x, f_y) = (0,$

$10.5\lambda)$, the conventional EM with two symmetrically distributed segments, which consist of seven functional units, is established based on the GSL. Furthermore, the optimized EM is obtained by introducing strong bridged couplings into the traditional EM. The simulated results of the intensity distribution of displacement fields around the focal point are shown in Fig. 2(c). The intersection of the white dashed lines is the focal point. Obviously, the manipulation capabilities for energy harvesting of the optimized EM with a dual-coupled resonator are better than those of the conventional EM. Figures 2(d) and 2(e) illustrate the normalized distributions of the wave intensity along the horizontal direction and the vertical direction at $x = 0$ and $y = 10.5\lambda$, as shown by the dashed white line markers in Fig. 2(c). According to the simulated results, which agree with theoretical predictions, an optimized EM with higher efficiency than the traditional EM can be observed distinctly.

To quantitatively characterize the ability of metasurfaces for focusing, the efficiency, η , based on energy density can be expressed as [27]

$$\eta = \frac{E_F}{E} = \frac{\int |A|^2 dl}{\int |A|^2 dx}, \quad (3)$$

where E_F is the power intensity of the full width at half maximum (FWHM) and E is the total power intensity along the x direction across the focal point. $|A|$ is the out-of-plane displacement, l is the FWHM, and x is the width

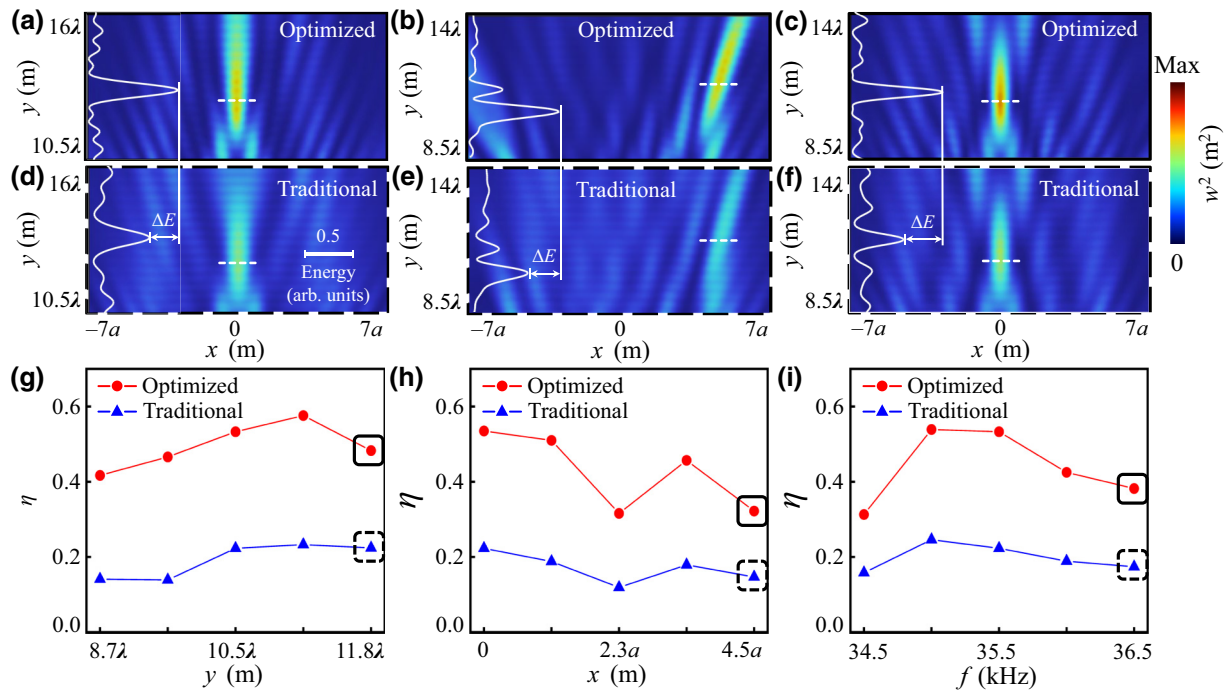


FIG. 3. Comparison of efficiency at different positions and frequencies. (a)–(f) Intensity distributions of displacement fields for different cases as follows: focal length $f_y = 11.8\lambda$ in (a),(d); arbitrary focusing with $f_x = 4.5a$ in (b),(e); and frequency at $f = 36.5$ kHz in (c),(f). White solid line is the normalized intensity curve corresponding to the white dashed lines at the focal point along the x direction in each inset of (a)–(f). (g)–(i) Variations of focusing efficiency with focal length f_y in range of 8.7λ – 11.8λ , arbitrary focusing with f_x in range of 0 – $4.5a$, and variable frequency in range of 34.5 – 36.5 kHz. Red and blue lines represent the efficiency of the optimized EM and traditional EM, respectively.

of the metasurface. According to Eq. (3), the efficiency of the EM with a dual-coupled resonator can be calculated as 53.3%, while that of the conventional local EM is only

22.3%. In comparison, the efficiency of the optimized EM is 239% higher than that of the traditional EM. The computational results are in good agreement with the simulation

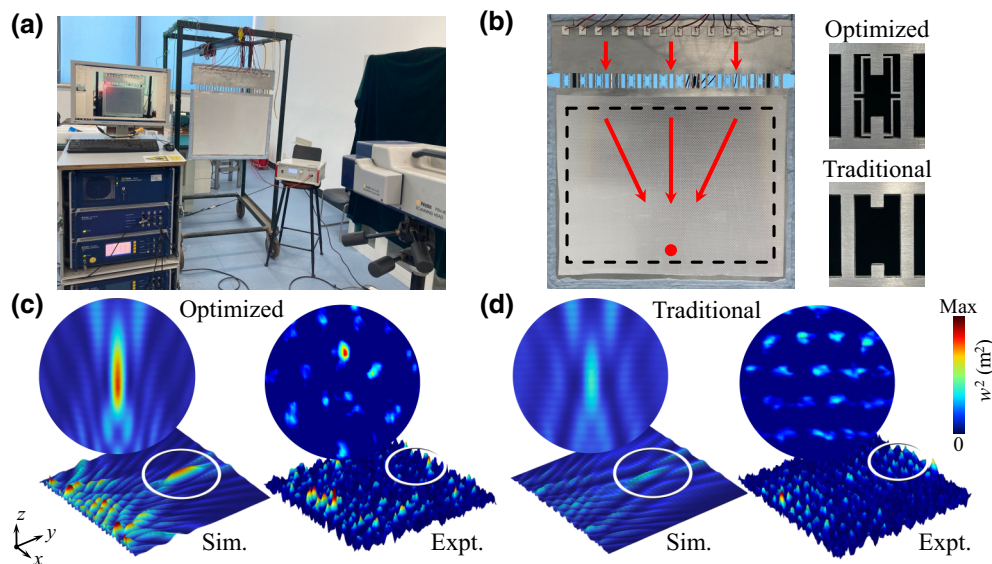


FIG. 4. Experimental setup and measured data. (a) Experimental setup. (b) Fabricated samples. Black dashed area is the defined measured region. Focal point is marked by the red solid circle. Insets show details of optimized and traditional functional units. (c),(d) Comparison of the simulation and experimentally measured results of optimized and traditional focusing, respectively.

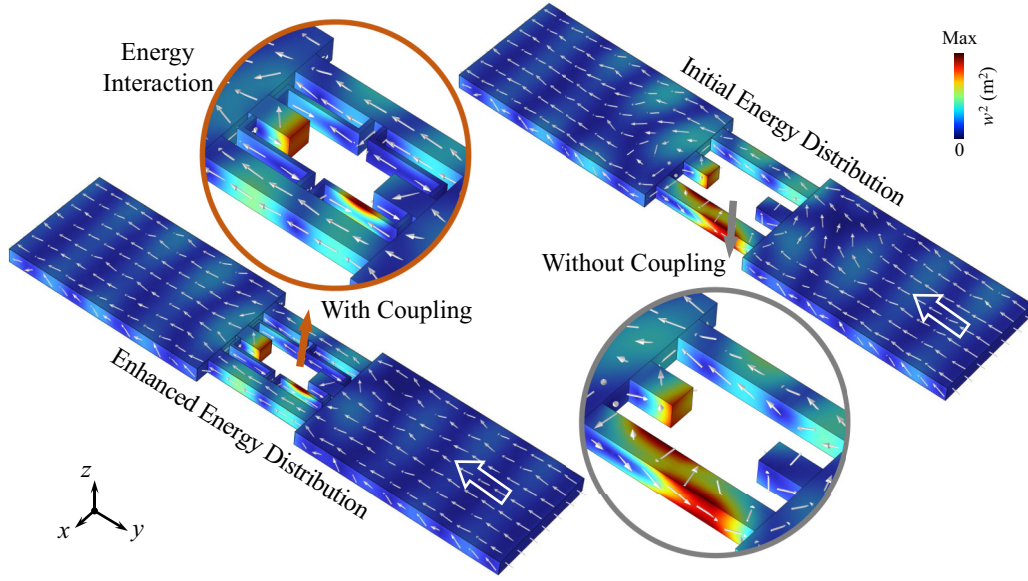


FIG. 5. Schematic of the power-flow distributions in functional units and details of energy interactions. White arrows indicate the local power-intensity vector in unit cells with $l = 10$ mm at 35.5 kHz.

predictions, and the feasibility of the optimized design to enhance efficiency is demonstrated numerically. To further demonstrate the focal abilities of both EMs, the efficiency curves of the two designs are compared for three different cases, as shown in Fig. 3. Specifically, Fig. 3(g) shows the efficiency of variable focal lengths in the range of 8.7λ – 11.8λ . Furthermore, the intensity distribution of displacement fields with a focal length of $f_y = 11.8\lambda$ is provided in Figs. 3(a) and 3(d). White solid lines illustrate the normalized distributions of the wave intensity corresponding to the white dashed lines at the focal point along the x direction. Obviously, the manipulation capabilities for energy harvesting of the optimized EM with a dual-coupled resonator are better than those of the traditional EM. The relationship between the FWHM and focal length is discussed in Appendix C. Likewise, Fig. 3(h) shows the efficiency of arbitrary focal points located at $(f_x, f_y) = (0-4.5a, 10.5\lambda)$. As an example, the intensity distribution of displacement fields corresponding to arbitrary focal points located at $(f_x, f_y) = (4.5a, 10.5\lambda)$ is provided in Figs. 3(b) and 3(e). As a result, the optimized EM with higher efficiency than that of the traditional EM can be predicted in the range of $9a \times 3.1\lambda$, according to Figs. 3(g) and 3(h). Moreover, to further evaluate the efficiency of the optimized EM with a dual-coupled resonator under incident waves with frequency fluctuation, an incident excitation in the frequency range of 34.5–36.5 kHz is created to observe the focusing displacement fields. The efficiency curves in Fig. 3(i) and an example in Figs. 3(c) and 3(f) suggest strongly that the efficiency of the optimized EM has reliable robustness against frequency fluctuation. Overall, these results indicate that the efficiency and performances of elastic metasurfaces are indeed enhanced by bridged couplings.

IV. EXPERIMENTAL METHODS

Experiments on the elastic focusing of flexural waves are conducted. The fabricated elastic plate samples (690×900 mm²) with a thickness of 6 mm and details are shown in Fig. 4(b). Considering the precision of samples and feasibility of processing, the elastic plates are fabricated through an electrical discharge machining (EDM) process with a resolution of 0.02 mm, through which air cavities are cut on an aluminum plate (6063 aluminum alloy) cube. The experimental measurements are made by using a custom two-dimensional (2D) vibrometry scanner system (PSV-400), as shown in Fig. 4(a). To absorb the reflection waves, the boundary of the samples is confined within colloidal absorbing foams with a thickness of 30 mm. The samples are suspended on a custom steel stand to avoid gravity interfering with the measurement results. Initial incident flexural waves with a width of about 630 mm along the x direction are generated from 14 electronically controlled strain gauges of the same size equally spaced in a longitudinal sequence. A normal incidence of $\theta_i = 0^\circ$ at 35.5 kHz is selected in our example. To map the 2D energy fields of out-of-plane displacements, a 630×650 mm² region with an appropriate offset from the metasurfaces (~ 20 mm) is covered with reflective stickers to improve the signal level of the laser vibrometer.

TABLE I. Material properties.

Material	Elastic modulus, E (GPa)	Poisson ratio, ν	Mass density, ρ (kg m ⁻³)
Aluminum	70	0.33	2700

TABLE II. Geometric parameters (unit: mm).

	a	b	c	d	e	h	l	m	n	t	L	D	H
Optimized	45	6	6	22	2	40	3–19	3.5	18	1	80	530	6
Traditional	45	6	6	22	–	40	3–19	–	–	–	80	530	6

A defined $600 \times 540 \text{ mm}^2$ measured region is meshed by equally spaced probing points with a center-to-center spacing of $5 \times 3 \text{ mm}^2$, as shown in the black dashed area in the inset of Fig. 4(b). A vibrometer controller (Polytec OFV-5000) with a scanning head (Polytec PSV-400) is used to obtain the distribution of out-of-plane displacements on the surface of samples by sweeping over the 2D area with a point-by-point measurement. At each probing position, the normalized value of the measured amplitude signals is recorded. The simulated and experimentally measured focusing fields are shown in Figs. 4(c) and 4(d), respectively. Results show that the experimentally measured data roughly agreed with the simulation. Some standing-wave-like antinodes are observed. These are mainly due to the perfectly matched layers (PML) not being able to absorb the elastic waves perfectly at the boundary. Moreover, the quality of the initial incident bending elastic waves excited by piezoelectric sheets is also an important factor that affects the experimental phenomenon. It can be observed that the optimized EM with a dual-coupled resonator preserves a relatively focal elastic wave field after passing the metasurfaces, enabling greater high-energy focusing with significantly suppressed side lobes.

V. CONCLUSIONS

We experimentally demonstrate high-efficiency elastic wave control of the EM with a dual-coupled resonator for energy harvesting based on bridged couplings. Efficiency

as high as 53.3% is observed. The enhanced efficiency of the optimized EM is realized to be 239% higher than the efficiency of the traditional local GSL devices. In addition, the robustness of the optimized high efficiency against variation of focal point and frequency fluctuations of the incident waves are realized. To introduce directly more effective coupling features easily, more reliable design ideas for multifunctional EMs need to be further explored. The given coupling design is expected to further promote practical applications of highly efficient energy harvesting and high-resolution elastic target signal perception.

Data that support the findings of this study are available from the corresponding author upon reasonable request.

ACKNOWLEDGMENTS

This work is supported by the Natural Science Foundation of China (Grant No. 12072221), the Fundamental Research Funds for the Central Universities (Grant No. 2013017), and the Ten Thousand Talents Program.

The authors have no conflicts of interest to disclose.

APPENDIX A: DISTRIBUTIONS OF POWER FLOW IN FUNCTIONAL UNITS

To uncover the highly efficient mechanisms, the distribution of power flow is analyzed inside functional units of an optimized EM with a dual-coupled resonator and a traditional EM. As shown in Fig. 5, a random parameter

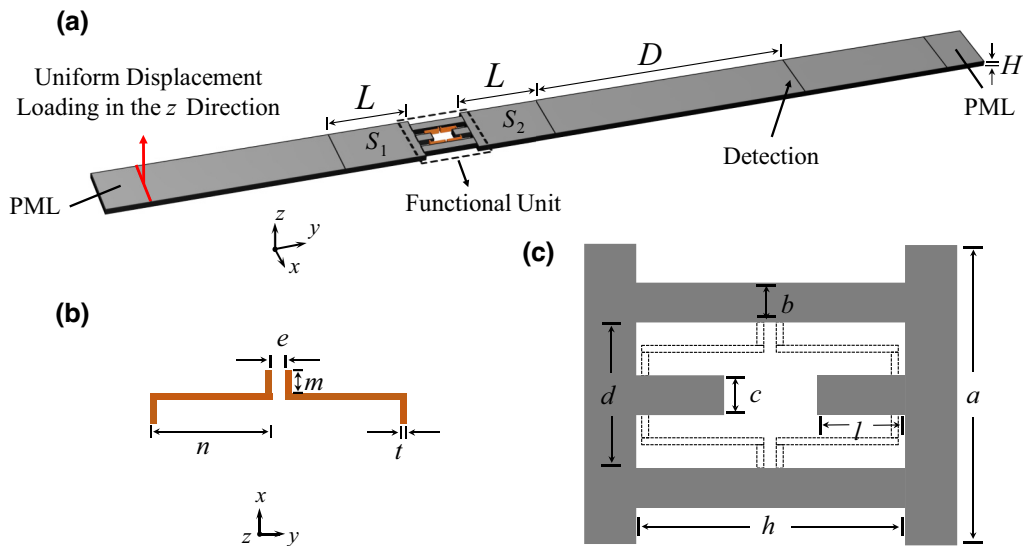


FIG. 6. Schematic diagram. (a) Strip model. (b) Bridged couplings. (c) Functional unit.

for both oscillators is selected to be $l = 10$ mm for further comparison under the input incentive at $f = 35.5$ kHz. In the conventional unit cell, energy cannot tunnel between mass oscillators. The components of the energy-flow vector exist in undesired directions. Consequently, energy cannot be focused efficiently on the target in the far field. Whereas, in the optimized unit cell with couplings, coupling bridges between the oscillators transmit the twisting moment from the oscillator to the neighboring links. A smoother and more stable energy flow is obtained to improve the efficiency of the EM based on the vibrational-energy interaction in the coupled bridge tunnels.

APPENDIX B: EVALUATION OF FUNCTIONAL UNITS

To evaluate the phase shift of flexural waves, the strip model is established. The properties and geometric parameters of the materials are shown in Tables I and II, respectively. As shown in Fig. 6(a), a unit-length load with an amplitude of 10 N m^{-1} in the z direction is applied on the left side of the model as an initial excitation to generate the incident wave. A probe line is placed in the far field to detect the displacement phase shift of the z component of the flexural wave transmitted through the functional units.

TABLE III. FWHM corresponding to different focal lengths (FLs).

FL	2λ	4.3λ	6.5λ	8.7λ	11λ
FWHM	0.30λ	0.37λ	0.43λ	0.70λ	0.85λ

The transmission ratio is calculated as follows:

$$T = \frac{\iint_{S_2} |A| ds}{\iint_{S_1} |A| ds},$$

where $|A|$ is the out-of-plane displacement, and the S_1 and S_2 regions are areas of equal size before and after the functional unit, respectively, as shown in Fig. 6(a).

APPENDIX C: RELATIONSHIP BETWEEN FWHM AND FOCAL LENGTH OF AN OPTIMIZED EM

To evaluate the relationship between the FWHM and focal length of the optimized EM, five focal-length values roughly equidistantly distributed in the range 2λ – 11λ are selected for further analysis. FWHMs corresponding to different focal lengths are shown in Table III. The variations of the focal lengths and FWHMs are consistent within the capability of the GSL. The intensity distributions of displacement fields and the corresponding curves of horizontal energy distribution are obtained, as shown in Fig. 7. Obviously, larger side lobes occur in the focused target

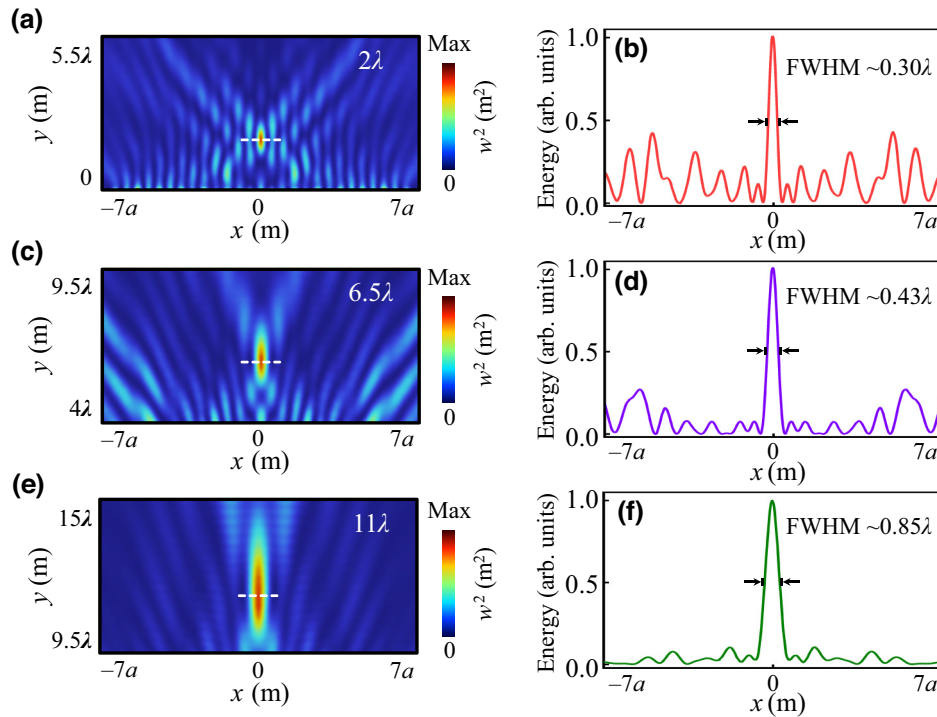


FIG. 7. FWHMs of different focal lengths. (a) Intensity distributions of displacement fields corresponding to the focal length as 2λ . (b) illustrations a curve of horizontal energy distribution with $\text{FWHM} = 0.3\lambda$ of focal points at 35.5 kHz. (c)–(f) Intensity distributions of displacement fields to the focal length as 6.5λ and 11λ at 35.5 kHz, corresponding to the $\text{FWHM} = 0.43\lambda$ and 0.85λ , respectively.

field as the focal length decreases. This means that the efficiency of energy focusing is reduced in EMs with a smaller focal length. The efficiency of the optimized EMs with a focal length of 2λ is only 20.1%. If the focal length is too small, beyond the capability of the GSL, for example, the focusing efficiency will decay sharply to less than 5%, corresponding to a focal length of 1.5λ . Therefore, appropriate working distances should be considered when designing energy-harvesting devices in practical applications.

-
- [1] T. Yang, X. Bai, D. Gao, L. Wu, B. Li, J. T. L. Thong, and C. Qiu, Invisible sensors: Simultaneous sensing and camouflaging in multiphysical fields, *Adv. Mater.* **27**, 7752 (2015).
- [2] J. Zhao, B. Li, Z. N. Chen, and C.-W. Qiu, Redirection of sound waves using acoustic metasurface, *Appl. Phys. Lett.* **103**, 151604 (2013).
- [3] J. Zhao, B. Li, Z. Chen, and C.-W. Qiu, Manipulating acoustic wavefront by inhomogeneous impedance and steerable extraordinary reflection, *Sci. Rep.* **3**, 2537 (2013).
- [4] W. Sha, Topology-optimized thermal metamaterials traversing full-parameter anisotropic space, *npj Comput. Mater.* **8**, 1 (2022).
- [5] P. Wang, F. Casadei, S. H. Kang, and K. Bertoldi, Locally resonant band gaps in periodic beam lattices by tuning connectivity, *Phys. Rev. B* **91**, 020103 (2015).
- [6] P. Wang, Y. Zheng, M. C. Fernandes, Y. Sun, K. Xu, S. Sun, S. H. Kang, V. Tournat, and K. Bertoldi, Harnessing Geometric Frustration to Form Band Gaps in Acoustic Channel Lattices, *Phys. Rev. Lett.* **118**, 084302 (2017).
- [7] Y. Long, J. Ren, and H. Chen, Intrinsic spin of elastic waves, *Proc. Natl. Acad. Sci. U. S. A.* **115**, 9951 (2018).
- [8] C. Yang, Y.-T. Tan, H. Chen, and J. Ren, Real spin angular momentum and acoustic spin torque in a topological phononic crystal, *J. Appl. Phys.* **129**, 135106 (2021).
- [9] Y. Long, D. Zhang, C. Yang, J. Ge, H. Chen, and J. Ren, Realization of acoustic spin transport in metasurface waveguides, *Nat. Commun.* **11**, 4716 (2020).
- [10] C. Yang, T. Liu, J. Zhu, J. Ren, and H. Chen, Surface-Acoustic-Wave Computing of the Grover Quantum Search Algorithm with Metasurfaces, *Phys. Rev. Appl.* **15**, 044040 (2021).
- [11] P. Wang, L. Lu, and K. Bertoldi, Topological Phononic Crystals with One-Way Elastic Edge Waves, *Phys. Rev. Lett.* **115**, 104302 (2015).
- [12] B. Deng, P. Wang, Q. He, V. Tournat, and K. Bertoldi, Metamaterials with amplitude gaps for elastic solitons, *Nat. Commun.* **9**, 3410 (2018).
- [13] Z.-N. Li, B. Yuan, Y.-Z. Wang, G.-S. Shui, C. Zhang, and Y.-S. Wang, Diode behavior and nonreciprocal transmission in nonlinear elastic wave metamaterial, *Mech. Mater.* **133**, 85 (2019).
- [14] L. Ning, Active control of elastic metamaterials consisting of symmetric double Helmholtz resonator cavities, *Int. J. Mech. Sci.* **153**, 287 (2019).
- [15] Z.-N. Li, Y.-Z. Wang, and Y.-S. Wang, Nonreciprocal phenomenon in nonlinear elastic wave metamaterials with continuous properties, *Int. J. Solids Struct.* **150**, 125 (2018).
- [16] Y.-Z. Wang and M. Kuna, General solutions of mechanical-electric-magnetic fields in magneto-electro-elastic solid containing a moving anti-plane crack and a screw dislocation, *Z. fur Angew. Math. Mech.* **95**, 703 (2015).
- [17] Z. Lin, W. Xu, C. Xuan, W. Qi, and W. Wang, Modular elastic metasurfaces with mass oscillators for transmitted flexural wave manipulation, *J. Phys. D: Appl. Phys.* **54**, 255303 (2021).
- [18] N. Yu, P. Genevet, M. A. Kats, F. Aieta, J.-P. Tetienne, F. Capasso, and Z. Gaburro, Light propagation with phase discontinuities: Generalized laws of reflection and refraction, *Science* **334**, 333 (2011).
- [19] H. Zhu, T. F. Walsh, and F. Semperlotti, Total-internal-reflection elastic metasurfaces: Design and application to structural vibration isolation, *Appl. Phys. Lett.* **113**, 221903 (2018).
- [20] T. Yang, Experimental evidence of high-efficiency nonlocal waterborne acoustic metasurfaces, *Adv. Eng. Mater.*, 2200805 (2022).
- [21] H. Xie and Z. Hou, Nonlocal Metasurface for Acoustic Focusing, *Phys. Rev. Appl.* **15**, 034054 (2021).
- [22] L. Quan and A. Alù, Hyperbolic Sound Propagation over Nonlocal Acoustic Metasurfaces, *Phys. Rev. Lett.* **123**, 244303 (2019).
- [23] L. Quan and A. Alù, Passive Acoustic Metasurface with Unitary Reflection Based on Nonlocality, *Phys. Rev. Appl.* **11**, 054077 (2019).
- [24] Y. Li, X. Jiang, B. Liang, J. Cheng, and L. Zhang, Metascreen-Based Acoustic Passive Phased Array, *Phys. Rev. Appl.* **4**, 024003 (2015).
- [25] H. Zhu, S. Patnaik, T. F. Walsh, B. H. Jared, and F. Semperlotti, Nonlocal elastic metasurfaces: enabling broadband wave control via intentional nonlocality, *Proc. Natl. Acad. Sci. U. S. A.* **117**, 26099 (2020).
- [26] H.-T. Zhou, W.-X. Fu, Y.-F. Wang, and Y.-S. Wang, High-Efficiency Ultrathin Nonlocal Waterborne Acoustic Metasurface, *Phys. Rev. Appl.* **15**, 044046 (2021).
- [27] Y.-Q. Liu, High numerical aperture and large focusing efficiency metalens based on multilayer transmitarray elements, *Opt. Lasers Eng.* **147**, 106734 (2021).